which should be cited to refer to this work.

$Ba_{0.5}Sr_{0.5}Co_{0.8}Fe_{0.2}O_{3-\delta}$ (BSCF) feedstock development and optimization for thermoplastic forming of thin planar and tubular oxygen separation membranes

Mehdi Salehi[a,b], Frank Clemens[a], Ewald M. Pfaff[c], Roberto M. Junior[d], Carlos P. Bergmann[d], Stefan Diethelm[e], Christoph Neururer[b], Thomas Graule[a] and Bernard Grobéty[b]

[a]Laboratory for High Performance Ceramics, Empa, Swiss Federal Laboratories for Materials Science and Technology, Ueberlandstrasse 129, CH-8600 Duebendorf, Switzerland

[b]The Fribourg Center for Nanomaterials (FriMat) and Department of Geosciences, University of Fribourg, Pérolles Ch. du Musée 6, CH-1700 Fribourg, Switzerland

[c] Institute for Materials Applications in Mechanical Engineering, RWTH Aachen University, Nizzaallee 32, 52072 Aachen, Germany

[d] Department of Materials, Federal University of Rio Grande do Sul, 90035-190 PoA-RS, Brazil

[e] Industrial Energy System Laboratory (LENI), IGM, Ecole Polytechnique Fédérale de Lausanne, Station 9, 1015 Lausanne, Switzerland

Corresponding author: Laboratory for High Performance Ceramics, Empa, Swiss Federal Laboratories for Materials Science and Technology, Ueberlandstrasse 129, CH-8600 Duebendorf, Switzerland.

Tel.: +41 58 765 4821

Fax: +41 58 765 4150

Email address:

Frank Clemens: Frank.clemens@empa.ch

Mehdi Salehi : chemehdi3333@gmail.com

Abstract

This paper presents the processing steps for producing thin planar and tubular oxygen separation membranes by thermoplastic forming of $Ba_{0.5}Sr_{0.5}Co_{0.8}Fe_{0.2}O_{3-\delta}$ (BSCF) with polystyrene (PS) and stearic acid (SA) as binder. The influence of powder content on the shape stability of thin membranes (tubular and planar structures) during the thermoplastic processing route was investigated. The effect of powder content on mixing torque and the rheological behavior were investigated. The effect of the powder content could be analytically described using the model proposed by Frankel and Acrivos. The deformation of free standing green bodies was investigated using disks. The result showed that increasing the powder content is remarkably effective to minimize the deformation of the membrane during the thermal debinding step. By using a high powder content (60 vol. %) and a multicomponent binder system composed of PS, SA and paraffin wax (PW), it was possible to achieve disks and thin wall tubular structures without deformation after sintering. Using capillary rheometer an unexpected decrease in the total extrusion pressure was measured for the feedstock containing PW. The change in apparent activation energy between 800-1000°C **was not related to the membrane properties.**

Keywords: thermoplastic forming, BSCF, shape stability, binder system, oxygen permeation flux

1. Introduction

Mixed ionic–electronic conducting (MIEC) perovskite-based materials are being used in a wide range of applications for instance as membranes in oxygen separation systems, as electrolyte materials in solid oxide fuel cells and as membrane reactor for the partial oxidation of methane to syngas [1, 2]. Material properties required for such applications should have a

high oxygen permeability as well as sufficient chemical and thermal stability at defined operating conditions.

Among MIEC oxides, $Ba_{0.5}Sr_{0.5}Co_{0.8}Fe_{0.2}O_{3-\delta}$ (BSCF) has been shown to be one of the most promising materials with a high oxygen permeation flux and phase as well as chemical stability at high enough temperatures [3-9].

Depending on wall thickness, oxygen permeation through a MIEC membrane is controlled either by surface reaction kinetics or bulk diffusion across the membrane. **For membranes with a significant lager thickness in relation to their characteristic thickness *(L>>Lc)*,** bulk diffusion is rate controlling and the oxygen permeation flux is inversely proportional to the membrane thickness. Decreasing the membrane thickness in this regime will increase the oxygen permeation flux. For $L << Lc$ however, surface reactions become the rate-controlling step. The oxygen flux in this case does not depend on wall thickness and remains constant also when further reducing the membrane thickness [10] .

The design of a successful air separation unit highly depends on choosing a membrane geometry, which allows to obtain the highest membrane surface area. Tubular, hollow fibers, and multi-channel monoliths configurations are thereby superior to planar designs[11]. Nevertheless, planar membranes are the most widely membrane configuration used to investigate the performance of MIEC materials at the laboratory scale, but sealing at high temperature and the small surface area are important handicaps **for oxygen permeability measurements**. Hollow fibers have much larger membrane surface area, but poor mechanical stability is a serious limiting factor. Sealing of multichannel monoliths with small channels is also problematic. The most advantageous geometry have designs based on tubular configurations, which simplify sealing at high temperature by keeping the two sealing ends in the cold zone, and also is expected to show the desired mechanical stability.

A detailed discussion on the conceptual design for full-scale air separation units showed that tubes are better suited than hollow fibers or flat plate multi-channel monoliths [11, 12].

Thermoplastic forming is the method of choice to produce thin-walled tubes with different diameters [13] . Extrusion, injection molding as well as warm pressing are the most common thermoplastic forming techniques [14, 15]. Clemens and Graule [16] used thermoplastic extrusion to prepare thin-walled zirconia tubes of 5 mm in diameter and 200 µm wall thickness. Trunec [13] used thermoplastic extrusion for the preparation of dense thin-walled tubes of roughly 10 mm in diameter with a wall thickness of around 300 µm. Recently, ther-

moplastic extrusion has been applied mainly by two groups to produce tubular membranes using perovskite materials [17-19].

Thermoplastic processing requires a feedstock composed of the ceramic powder, a binder and a plasticizer. The organic components give the desired flow properties during mixing and shaping, which is typically done at a temperature between 60 and 200°C depending on the organics used. The next step is the shaping process. The binder has an important role in thermoplastic shaping as a temporary phase which gives flowability and plasticity to the feedstock during the shaping process. Before sintering, the binder has to be removed through thermal or solvent-thermal debinding.

For thermoplastic ceramic processing, different polymeric binder systems are discussed in the literature [20]. The application of thermoplastic process for the manufacture of MIEC ceramic membranes requires the development of a suitable feedstock composition. In this study, thermoplastic forming of BSCF membrane with feedstock based on polystyrene (PS), stearic acid (SA) and paraffin wax (PW) was investigated. The effect of the feedstock composition and process parameters on the evolution of torque during high shear mixing, the shape stability during debinding as well as on densification during sintering was investigated.

2. Experimental procedure

2.1 Powder and binder characterization

Commercially available $Ba_{0.5}Sr_{0.5}Co_{0.8}Fe_{0.2}O_{3-\delta}$ (BSCF) powder (Treibacher, Austria), with a median particle size of 3.8 μm and a specific surface area of 1.55 m^2/g was used. Polystyrene (type 648, Dow Company, Switzerland) and paraffin wax (76231 Fluka AG, Switzerland) were used as binder, with additions of stearic acid as a surfactant (Fluka AG, Switzerland; Table 1). Thermogravimetric analysis (TGA) (TGA/SDTA851e, Mettler-Toledo, Switzerland) from 30 to 600°C was carried out to investigate the thermal debinding characteristics of binders (heating rate: 15°C/min, air atmosphere with a flow rate of 50 cm^3/min).

Prior to compounding, the BSCF powder was pre-coated with stearic acid. The stearic acid was chosen to achieve better interaction between the hydrophobic binder and the hydrophilic surface of the ceramic particle, the coating procedure is described in more detail elsewhere [21]. The particle size distribution of the powders was measured with a laser diffraction analyzer (LS230, Beckman-Coulter, USA) in a toluene suspension. The specific surface area (SSA) of the powders was determined from a five-point N_2 adsorption isotherm obtained from

BET measurements (Beckman-Coulter SA3100, Beckman-Coulter, USA). The densities of the powders were measured by He-pycnometer (Micromeritics, AccuPyc 1330, USA).

2.2 Feedstock preparation

The feedstocks (Table 2) were prepared with different BSCF powder contents in a high shear mixer (HAAKE PolyLab Mixer, Rheomix 600, Thermo Scientific, Germany) equipped with a pair of roller blades. The torque was recorded as a function of mixing time. The mixing was carried out in a two-step sequence in order to improve homogeneity and reduce particle agglomeration [21]. In the first step, the mixing was performed at 180°C with 10 rpm for 30 min. In a second step, mixing was continued at 160°C with 10 rpm for 150 min until the torque stabilized, which is an indication for a homogeneous feedstock mixture. The homogeneity of each feedstock was determined through density measurements of three aliquots of the same feedstock using He-pycnometer (Micromeritics, AccuPyc 1330, USA). The rheology of the feedstocks was analyzed with a twin-bore capillary rheometer (RH7-2, Malvern, Germany). The total extrusion pressure was measured using a long capillary (L/D = 16). The die entry pressure drop was measured with a short die length of 0.26 mm of the same diameter, following the Cogswell theory [22]. Feedstock 5 was only used to compare rheological properties of the feedstock. A detailed sketch of both capillary dies is shown in Figure 1.

Table 2

Figure 1

2.3 Membrane Preparation

Planar membranes were prepared by warm pressing [23]. The feedstocks were loaded into a steel die with heating mantle and uniaxially pressed at 30 KN and 165^{o}C for 30 min to form disk-shaped membranes, approximately 28 mm in diameter. Tubular membranes were extruded through a 10 mm diameter and 1 mm wall thickness die using a capillary rheometer (RH7-2, Malvern, Germany). The velocity of the piston and temperature were constant during the extrusion (V_{piston} = 4.0 mm/min, T = 180°C). As expected, the change in the composition of feedstock 6 resulted in a much lower viscosity. Therefore, it was not possible to extrude feedstock 6 under the same conditions. The velocity of the piston and temperature were changed to V_{piston} = 50 mm/min and T = 140°C.

2.4 Debinding and sintering

The elimination of the organic polymers was performed by thermal debinding. A slow heating program was applied up to 600°C in air. The debinding schedule was devised from thermogravimetric analysis of the feedstocks. Binder removal for feedstock 6 was performed by a wicking debinding process followed by a thermal treatment. The wicking debinding was carried out at 150°C and 4 h holding time. This additional step of debinding was performed in order to remove PW. Planar and tubular membranes were sintered at 1000°C for 2 h in air, using a heating rate of 1°C /min. The densities of the sintered samples were measured by the Archimedes method. The cross-section of the sintered tubular membranes was examined by scanning electron microscopy (SEM, Tescan TS51368M).

Electron backscatter diffraction (EBSD) was used to analyze the microstructure of the sintered membranes. The sintered samples were polished to achieve a smooth strain-free surface. All EBSD data were collected using a Philips® FEI XL30 SFEG Sirion SEM equipped with an EDAX® (TSL) OIM system. The best results were obtained with an accelerating voltage of 15 kV and a probe current of 20 nA, a sample tilt 70° and a working distance of 15mm. To reduce the measuring time, the step size (=the resolution) and analyzed area were adjusted to average grain size. An area of 120 μm x 120 μm was mapped with a step size of 0.25 μm/step.

2.5 Permeation measurements

The permeation experiments set-up was described previously [17, 23]. The sintered disc membranes (23 mm in diameter and 0.6 mm in thickness) were clamped between two alumina tubes and sealed using gold rings and paste. The surface of the samples was polished manually before permeation measurement. air (350 Nml/min) was fed into the lower compartment, and argon (99.998%) (100 Nml/min) was used as sweep gas in the upper one. The outlet gas composition was analyzed with a gas chromatograph (GC) (Varian Inc.) equipped with a molecular sieve, 5 Å capillary columns and a Thermal Conductivity Detector (TCD) detector. The outlet flux was measured using a digital flow-meter (Varian Inc.). The amount of N_2 in the outlet gas was systematically measured in order to detect eventual leakage. This amount always remained small below 2%. The sample was first heated up to 1000°C to soften the gold rings and ensure a good seal. The temperature was then decreased step-wise, with permeation measurements made every 25 ºC. The flux was measured after equilibration of the sample. Flux measurements were repeated up to 7 times for each condition to check the reproducibility.

3 Results and Discussion

3.1 Experimental results for feedstock 1-4

3.1.1 Powder and binder characteristics

The properties of the uncoated and coated BSCF powders are presented in Table 3. The data clearly show the steric stabilization effect of stearic acid.

Table 3

The agglomeration factor, F_{ag} in Table 3, indicating the state of agglomeration of the powder, was calculated from the results of BET and particle size distribution analysis using the following equation:

$$F_{ag} = \frac{d_{50} \times \rho \times S_{BET}}{6} \qquad (1)$$

where, d_{50}, ρ and S_{BET} are median particle size, powder density and specific surface area, respectively. As shown in Table 3, F_{ag} decreases by a factor of 2, and as expected SA works as a steric stabilization agent.

The thermal decomposition behavior of polymeric binders was investigated by TG analysis (**Fig. S1, supporting figures**). Stearic acid (SA) and paraffin wax (PW) show a rapid thermal decomposition. It can be seen from Figure S1 that SA and PW decompose at lower temperatures than PS. The mass loss starts at around 190°C and is completed by 450°C. In contrast, the mass loss of the PS begins at about 290 °C and no trace of the polymer can be determined after 500 °C.

3.1.2 Feedstock preparation

Figure 2 shows the evolution of the torque during mixing of the feedstocks for different powder contents. In all feedstocks, an increase of the torque after around 5 min corresponds to the filling of the powder inside the mixing chamber. The final steady state torque value, which is proportional to the viscosity of the feedstock [24], increases with increasing powder content.

Figure 2

The evolution of the torque with mixing time is distinctively different between mixtures with low and high powder content. The torque, for each of the feedstocks 1 and 2, decreases monotonously to the final steady state value. For feedstocks 3 and 4, however, the viscosity

goes through a minimum before increasing to the final steady state value. The final increase of the torque could be explained by breaking down the agglomerates to smaller particles [25]. The agglomerates are the result of the previous coating with SA. The break down in feedstocks with low powder content seem not occur because there are fewer particle-agglomerate and agglomerate-agglomerate interactions, which may lead to the disintegration of the latter.

It is necessary to determine the critical powder content to optimize the powder content of binder-powder mixture. The critical powder content is generally defined as the concentration at which the powder particles are all in direct contact with each other forming a continuous network whereas the binder fills the spaces between the particles. Powder content higher than critical is characterized by a strong drop in plasticity, and the forming step becomes difficult. The critical powder content of 65.2 vol.% was determined for BSCF feedstock prepared with the PS by extrapolation of data to infinite torque = zero reciprocal torque (Fig.3) [22].

Figure 3

The measured torque values and the extrapolated value for infinite torque of the BSCF feedstocks are well described by the model proposed by Frankel-Acrivos (Fig. 4) [26]. Although a low viscosity of the feedstock is an advantage in the thermoplastic processing, an excess of binder should be avoided because it leads to deformation during debinding [27]. In this study, the extrusion pressure for feedstocks with a powder content > 54 vol. % resulted in the mechanical deformation of the tubular die. Previous thermoplastic processing experiments with different perovskite and ZrO_2 powders have shown that typically powder content between 52 and 54 vol. % is sufficient to produce stable tubular-shapes after sintering [13, 16-19]. For the preparation of tubular membranes using perovskite powders, the optimum powder content was reported to be around 51vol.% for the extrusion of straight tubes with outer diameter of 4.8–5.5 mm and thickness of 0.25–0.47 mm [19].

Figure 4

3.1.3 Characterization of the feedstocks

Table 4 lists the theoretical and measured densities of the feedstocks. The low deviation value indicates the good homogeneity of each feedstock. The measured values are consistent with the theoretical density calculated by the rule of mixture.

Table 4

The apparent shear viscosity versus shear rate of the feedstocks with 52, 54, and 56 vol. % powder content at 180°C is shown in Figure 5. The temperature was adjusted to the temperature used in the extrusion experiment. It can be seen that with increasing the shear rate the viscosity decreases, which indicates a shear thinning behavior of the feedstocks. There is not a significant difference in viscosity between feedstocks with 54 and 56 vol. %, nevertheless the small change in viscosity was enough to push the extrusion pressure above the yield stress of the die.

Figure 5

Changes of die entry pressure ($P_{entrance}$ for orifice capillary in Fig. 1) and total extrusion pressure (P_{total} for long capillary in Fig. 1) for feedstocks 2-4 as a function of shear rate are shown in Figure 6. It can be seen that both pressures increase with the shear rate and the powder content. This behavior, however, was expected to reflect the response to reducing the viscosity of the feedstock.

Figure 6

The debinding cycle has been designed using the results of the thermogravimetric measurements (**Fig. S2, supporting figures**). It can be seen that there is a one-step mass loss in TGA for feedstocks 1-4. The mass loss starts at temperatures around 290°C, and the removal is completed at about 550°C for all feedstocks. From the TGA results, the debinding cycle was designed, as shown in Figure S3 (**supporting figures, P1**) and feedstock 2 (52 vol. % BSCF) was chosen for fabricating the membranes. Because there was no major mass loss observed up to 250°C; a heating rate of 1°C/min was applied up to this temperature. As can be seen in Figure S2 the mass loss proceeds rapidly between 300 and 400°C, which translates into a rapid internal gas pressure build-up and may introduce defects into the sample. Thus a slow debinding rate of 0.5°C /min was applied across this temperature range to minimize defect formation.

For the final heating step up to 600°C a ramp of 1 °C/min (Fig. S3, P1) was initially chosen, which led however to deformation and cracking of the tubes. Extending the slower heating rate to 400°C gave the better results. Nevertheless, even using a slow heating rate (Fig. S3, P2) slight deformation for tubes could not be avoided. To get a better insight into the deformation mechanisms during debinding, experiments with flat disks manufactured from the feedstocks1-4, were performed. Crack-free green bodies were placed on a refractory sup-

port with a span length of 20 mm in the furnace (Fig.7). The thickness and diameter of the disks were around 0.80 and 28 mm, respectively.

Figure 7

The thermal debinding process can be split into four stages: 1) softening of the binder, 2) melting, 3) beginning of decomposition, and 4) migration of the decomposition products. To analyze the deformation induced in each of the individual stages, the debinding program (Fig. S3, P2) was interrupted at various stages. The temperatures chosen for this purpose were 80ºC, 100ºC, 250ºC and 600ºC. The photographs of flat membrane made from different feedstocks during binder removal at different temperatures are shown in Figures 7. Visual deformation of the samples occurred in the early stages as a consequence of softening of the polymer binder.

As shown in Figures 7, the disks preserved their shape after being heated at 80°C, a temperature which is above the melting temperature of SA but below the glass transition temperature of the PS. Samples heated to 100°C, i.e. around the glass transition temperature of the PS used, showed the first signs of deformation, which were particularly significant for the samples manufactured from feedstock 1 (48 vol. % powder content). Deformation became obvious for all samples when heated at 250°C. This temperature is below the onset temperature for the decomposition of pure PS but around the one of stearic acid (**Fig. S1 and S2**). Such a deformation behavior has been not observed for other feedstocks made from $La_{0.6}Ca_{0.4}Fe_{0.75}Co_{0.25}O_{3-\delta}$, $La_{0.5}Sr_{0.5}Fe1_{-y}Ti_yO_{3-\delta}$ (y = 0, 0.2) and ZrO_2 with a powder content around 52 vol. % [16, 19]. This could be due to the strong catalytic activity of BSCF, which promotes the initial decomposition of the binder (**see Fig. S4 supporting figures, BSCF in feedstock 1 is replaced by ZrO_2**).

For the sample prepared with feedstock 1 (48 vol. % powder content), the deformation was so high that they were discarded. Figure 7 also demonstrates the deformation of the flat membranes at the end of the treatment e.g. after heating to at 600ºC, using a stepwise debinding program (**Fig.S3, P2**). It is evident that none of the membranes kept its initial shape, even the samples with 56 vol. % powder content. It has been reported [28-30] that for injection molded samples deformation at around the glass transition temperature is critical. Kipphut and German [28] reported that the shape loss during thermal debinding primarily occurs because of flow by viscous creep when the softening point is reached. High powder content minimizes

the deformation. The maximum powder content tested for BSCF, however, was still not sufficient to eliminate the viscoelastic behavior of the plates beyond the softening point. Nevertheless, it was possible to achieve simple planar structures (52 vol. % BSCF) on a flat substrate by optimizing the debinding program.

3.2 Optimization of feedstock

The powder content was, therefore, raised to 60 vol. % in the subsequent experiments. With increasing the powder content, however, the viscosity of feedstock increases which results in an increase in the extrusion pressure. A way to lower the pressure, while maintaining the powder content, is to add a major binder (backbone component) and a minor lubricating binder. The latter lowers the friction between the feedstock and the die wall and improves the flowability of the feedstock. Ideal candidates are waxes, which can be eliminated in early stages of debinding, leaving back open pores within the composite. The created open pores allow a rapid elimination of backbone polymer in the subsequent debinding step without introducing deformation or cracks in the sample. In addition, the feedstock based on paraffin wax has low viscosity and good fluidity**.**

The rheological behavior of PS-PW binder system was measured at a lower temperature (140°C) than those of PS system, due to the low melting temperature of PW. The addition of PW has a major effect on the mixing behavior of the feedstocks, as shown in Figure 4. The torque decreases significantly and therefore a much lower extrusion pressure is observed.

In contrast to feedstock 1-4, which show large differences between the die entry and the total extrusion pressure, the values for feedstocks 5 and 6 are almost the same. Whereas the die entry pressures between mixtures with and without PW are similar (Fig. 6 and 8), a dramatic reduction in the overall pressure with the addition of PW is observed. Lubrification of the die walls by PW, which promotes wall slipping, is most likely responsible for the lowering of the pressure. It is reported that a strong wall slipping causes a pressure drop across the die for molten polymers [31] (decreasing the P_{shear} or $P_{die\ land}$). Interestingly, feedstock 5 shows a nonlinear behavior of the extrusion pressure with high shear rate.

The different binders in feedstock 5 and 6 are eliminated in steps. Figure 9 shows the TGA and Derivative Thermogravimetric analysis (DTG) of the green bodies. Without wicking, the binder begins to decompose at about 185°C and completely remove at about 550°C through two mass loss stages. SA and PW start to decompose at around 185°C, with a DTG peak at 265°C.

Figure 8

Above 300°C, PS starts to decompose. With prior wicking, a single decomposition step is observed in the TGA and DTG curves, which represents the mass loss of the PS. During wicking debinding about, 2.66 wt. % of the primary polymer constituents are extracted. This indicates that about 60% of the initial PW and SA are removed. Previous results indicate that the extraction of around 35% PW and SA by wicking is sufficient to create the necessary porosity to eliminate the remaining polymer without failure in the samples [32].

The two step binder removal process, e.g. the combination of wicking (removing PW and SA) and thermal debinding (removing PS), were applied to both the tubular and the planar geometries made of feedstock 6. Figure 10 shows photographs of the disk and tubes after different processing steps, demonstrating that the addition of PW and the increase of the powder content promote the shape stability after debinding and sintering processes (with about 97% of a theoretical sintered density). Also, the micrograph of the cross-section of a tube sintered at 1000 °C/2 h is shown in Figure S5 in supporting material. **Figure 11 shows SEM images of the disk and tubular membranes sintered at 1000°C for 2h. The overall porosity determined by image analysis was about 11.3% and 10.8 % for the disk and tubular membranes, respectively. These values are in good agreement with those reported for BSCF disk-shaped membrane fabricated by warm pressing (the membranes prepared with feedstock 7) [23] and disk-shaped membranes prepared by uniaxial pressing (Treibacher, wet milled BSCF powder, sintered at 1000 ◦C for 12 h) [9].**

Figure 9

Figure 10

Figure 11

Figure 12 shows that the grain size distributions determined from the EBSD images are similar for planar and tubular membranes. The grain size distribution is respectively in the range of 0.3-12μm with a weighted average of 5μm for planar membrane and in the range of 0.4-7μm with a weighted average of 4.28μm for tubular membrane. Figure 13 shows that the lattice preferred orientation for both planar and tubular samples is very weak. In earlier work [23], it was also shown that there was no lattice preferred orientation for the membranes prepared with feedstock 7 (power content: 52 vol. %, binder system: PS-PEG).

Figure 12

Figure 13

3.3 Permeation measurements

The Arrhenius plot of the oxygen permeation flux for the membranes prepared with feedstock 6 (power content: 60 vol. %, binder system: PS-PW) and feedstock 7 (power content: 52 vol. %, binder system: PS-PEG) in the temperature range 800-1000°C is shown in Figure 14.

Between 900°C and 1000°C both samples have more or less the same permeation flux. Below 900°C, however, the sample prepared from feedstock 7 has considerably higher values. The slope in the Arrhenius plots changes at 900°C for both samples, indicating a change in the permeation mechanism. Below 900°C the apparent activation energy (44-46 kJ/mol) obtained from the slope in the Arrhenius plot is at the upper end of published values (Table 5), which are associated to bulk diffusion as rate limiting step. For the BSCF membranes, literature reports that the apparent activation energy for bulk diffusion is lower than that for surface-exchange kinetic**. Listing previous reported apparent activation energies (Table 5) suggests that the activation energy depends on membrane characteristics (e.g. thickness and surface conditions) and measurement conditions (e.g. pO2 in the sweep gas and type of sweep gas).**

Oxygen permeation through a dense ion-conducting membrane is a complex mechanism consisting of several resistances in series (see Fig. S6 in supporting material). In literature, the oxygen exchange kinetics on each surface of the membrane at low temperatures or the oxygen bulk diffusion at high temperatures have been mostly suggested as the rate limiting steps. Changing the operating conditions resulted in changing the rate limiting step from predominantly oxygen bulk diffusion to predominantly oxygen exchange kinetics and vice versa [33]. Gas-solid mass transfer (oxygen diffusion through the boundary layer adjacent to the membrane surface) as a possible rate limiting factor is usually neglected. Xu et al. modeled the influence of the oxygen permeation resistance and they conclude that it is jointly controlled by the surface exchange at the oxygen-lean side and the bulk diffusion [34].

As the argon flow rate was increased from 100 Nml/min to 225 Nml/min (see Fig.14, for membrane prepared with feedstock 6), the oxygen permeation flux increased but the change in the apparent activation energy above 900°C also disappeared. The increase of

sweep gas flow rate results in the reduction of the boundary layer adjacent to the membrane surface (R_{bl2} in Fig. S6 in supporting material), and also increases the driving force for oxygen permeation. An apparent activation energy of 38 kJ/mol was calculated over the complete temperature range (800-1000°C) for the argon flow rate of 225 Nml/min (Fig. 14). This seems to indicate that the change in apparent activation energy at high temperatures is not related to the membrane properties but corresponds to transport limitations through a boundary layer (R_{bl2}).This is consistent with the low apparent activation energy values calculated above 900°C (Fig. 14).

Figure 14

4. Conclusion

Tubular and flat membranes have been prepared by a thermoplastic forming method using a commercial BSCF powder, PS thermoplastic binder and SA as a surfactant. Coating of the powder by SA improved the rheology of the powder-polymer blend for thermoplastic forming. The torque measurement in terms of powder content indicated that the torque increased with increasing powder content. By steady state torque measurement of different feedstock the maximum theoretical powder content was calculated as 65.2 vol. %. The torque behavior in relation to powder content could be well described **by the model of** Frankel and Acrivos. Tubular membranes were deformed during the binder removal, even with a powder content of 56 vol. %. The deformation study of flat membranes revealed that powder content had a major effect on deformation of samples during thermal debinding, as expected it was observed that higher powder content resulted in lower deformation. Flat membranes without deformation can be produced with low powder content (52 vol. %) on a flat substrate. To produce tubular membrane, as the result, a new feedstock formulation based on a multicomponent binder system consists of PS-PW and high powder content (60vol. %) has been developed. With this optimized feedstock, defect-free thin tubular structures were achieved after sintering. The temperature dependence of the oxygen permeation flux shows that the change in apparent activation energy **at high temperatures** could not be due to the membrane properties.

References

[1] J. Sunarso, S. Baumann, J.M. Serra, W.A. Meulenberg, S. Liu, Y.S. Lin, J.C. Diniz da Costa, Mixed ionic–electronic conducting (MIEC) ceramic-based membranes for oxygen separation, Journal of Membrane Science, 320 (2008) 13-41.

[2] Q. Jiang, S. Faraji, D.A. Slade, S.M. Stagg-Williams, Chapter 11 - A Review of Mixed Ionic and Electronic Conducting Ceramic Membranes as Oxygen Sources for High-Temperature Reactors, in: S.T. Oyama, M.S.-W. Susan (Eds.) Membrane Science and Technology, Elsevier, 2011, pp. 235-273.

[3] Z. Shao, W. Yang, Y. Cong, H. Dong, J. Tong, G. Xiong, Investigation of the permeation behavior and stability of a Ba0.5Sr0.5Co0.8Fe0.2O3-[delta] oxygen membrane, Journal of Membrane Science, 172 (2000) 177-188.

[4] Z. Shao, G. Xiong, H. Dong, W. Yang, L. Lin, Synthesis, oxygen permeation study and membrane performance of a Ba0.5Sr0.5Co0.8Fe0.2O3-[delta] oxygen-permeable dense ceramic reactor for partial oxidation of methane to syngas, Separation and Purification Technology, 25 (2001) 97-116.

[5] H. Lu, J. Tong, Y. Cong, W. Yang, Partial oxidation of methane in Ba0.5Sr0.5Co0.8Fe0.2O3-[delta] membrane reactor at high pressures, Catalysis Today, 104 (2005) 154-159.

[6] H. Wang, C. Tablet, A. Feldhoff, J. Caro, Investigation of phase structure, sintering, and permeability of perovskite-type Ba0.5Sr0.5Co0.8Fe0.2O3-[delta] membranes, Journal of Membrane Science, 262 (2005) 20-26.

[7] J.F. Vente, S. McIntosh, W.G. Haije, H.J.M. Bouwmeester, Properties and performance of BaxSr1-xCo 0.8Fe0.2O3-δ materials for oxygen transport membranes, Journal of Solid State Electrochemistry, 10 (2006) 581-588.

[8] P. Zeng, Z. Chen, W. Zhou, H. Gu, Z. Shao, S. Liu, Re-evaluation of Ba0.5Sr0.5Co0.8Fe0.2O3-[delta] perovskite as oxygen semi-permeable membrane, Journal of Membrane Science, 291 (2007) 148-156.

[9] S. Baumann, F. Schulze-Küppers, S. Roitsch, M. Betz, M. Zwick, E.M. Pfaff, W.A. Meulenberg, J. Mayer, D. Stöver, Influence of sintering conditions on microstructure and oxygen permeation of Ba0.5Sr0.5Co0.8Fe0.2O3-[delta] (BSCF) oxygen transport membranes, Journal of Membrane Science, 359 (2010) 102-109.

[10] J. Sunarso, G.X. Wang, S. Liu, J.C. Diniz da Costa, V. Rudolph, Oxygen transport through dense BaBi0.05Sc0.1Co0.85O3−δ ceramic membrane, Chemical Engineering Science, 66 (2011) 2091-2097.

[11] J.F. Vente, W.G. Haije, R. Ijpelaan, F.T. Rusting, On the full-scale module design of an air separation unit using mixed ionic electronic conducting membranes, Journal of Membrane Science, 278 (2006) 66-71.

[12] M. den Exter, J.F. Vente, D. Jansen, W.G. Haije, Viability of mixed conducting membranes for oxygen production and oxyfuel processes in power production, Energy Procedia, 1 (2009) 455-459.

[13] M. Trunec, Fabrication of zirconia- and ceria-based thin-wall tubes by thermoplastic extrusion, Journal of the European Ceramic Society, 24 (2004) 645-651.

[14] R. Lenk, J. Adler, SiC platelet orientation in a liquid-phase-sintered silicon carbide composite formed by thermoplastic forming techniques, Journal of the European Ceramic Society, 17 (1997) 197-202.

[15] D. Galusek, J. Sedláček, R. Riedel, Al2O3–SiC composites prepared by warm pressing and sintering of an organosilicon polymer-coated alumina powder, Journal of the European Ceramic Society, 27 (2007) 2385-2392.

[16] F. Clemens, T. Graule, Thin Wall Ceramic Tubes by Extrusion of Thermoplastic-ZrO₂ Compounds, KEM Key Engineering Materials, 206-213 (2002) 425-428.

[17] S. Diethelm, J. Sfeir, F. Clemens, J. Van herle, D. Favrat, Planar and tubular perovskite-type membrane reactors for the partial oxidation of methane to syngas, Journal of Solid State Electrochemistry, 8 (2004) 611-617.

[18] M. Trunec, J. Cihlar, S. Diethelm, J. Van Herle, Tubular La0.7Ca0.3Fe0.85Co0.15O3–δ Perovskite Membranes, Part I: Preparation and Properties, Journal of the American Ceramic Society, 89 (2006) 949-954.

[19] D. Bayraktar, F. Clemens, S. Diethelm, T. Graule, J. Van herle, P. Holtappels, Production and properties of substituted LaFeO3-perovskite tubular membranes for partial oxidation of methane to syngas, Journal of the European Ceramic Society, 27 (2007) 2455-2461.

[20] M.R. Ismael, F. Clemens, T. Graule, M.J. Hoffmann, Effects of different thermoplastic binders on the processability of feedstocks for ceramic co-extrusion process, Ceramics International, 37 (2011) 3173-3182.

[21] J. Heiber, F. Clemens, T. Graule, D. Hülsenberg, Thermoplastic Extrusion to Highly-Loaded Thin Green Fibres Containing Pb(Zr,Ti)O3, Advanced Engineering Materials, 7 (2005) 404-408.

[22] F.J. Clemens, V. Wallquist, W. Buchser, M. Wegmann, T. Graule, Silicon carbide fiber-shaped microtools by extrusion and sintering SiC with and without carbon powder sintering additive, Ceramics International, 33 (2007) 491-496.

[23] M. Salehi, F. Clemens, E.M. Pfaff, S. Diethelm, C. Leach, T. Graule, B. Grobéty, A case study of the effect of grain size on the oxygen permeation flux of BSCF disk-shaped membrane fabricated by thermoplastic processing, Journal of Membrane Science, 382 (2011) 186-193.

[24] R. Supati, N.H. Loh, K.A. Khor, S.B. Tor, Mixing and characterization of feedstock for powder injection molding, Materials Letters, 46 (2000) 109-114.

[25] T. Hanemann, R. Heldele, T. Mueller, J. Hausselt, Influence of Stearic Acid Concentration on the Processing of ZrO2-Containing Feedstocks Suitable for Micropowder Injection Molding, International Journal of Applied Ceramic Technology, 8 (2011) 865-872.

[26] J. Heiber, F. Clemens, T. Graule, D. Hulsenberg, Influence of varying the powder loading content on the homogeneity and properties of extruded PZT-fibers, Key Eng Mat Key Engineering Materials, 368-372 PART 1 (2008) 11-14.

[27] Y. Li, L. Li, K.A. Khalil, Effect of powder loading on metal injection molding stainless steels, Journal of Materials Processing Technology, 183 (2007) 432-439.

[28] C.M. Kipphut, R.M. German, Powder selection for shape retention in powder injection molding, International Journal of Powder Metallurgy (Princeton, New Jersey), 27 (1991) 117-124.

[29] W.J. Tseng, D.M. Liu, Effect of processing variables on warping behaviours of injection-moulded ceramics, Ceramics International, 24 (1998) 125-133.

[30] W.J. Tseng, Warping evolution of injection-molded ceramics, Journal of Materials Processing Technology, 102 (2000) 14-18.

[31] S.G. Hatzikiriakos, K.B. Migler, Polymer processing instabilities : control and understanding, Marcel Dekker, New York, 2005.

[32] H. Soykan, Karaka, Y., Injection moulding of thin walled zirconia tubes for oxygen sensors, Advances in Applied Ceramics, 104 (2005) 285-290.

[33] X. Zhu, H. Liu, Y. Cong, W. Yang, Permeation model and experimental investigation of mixed conducting membranes, AIChE Journal, 58 (2012) 1744-1754.

[34] S.J. Xu, W.J. Thomson, Oxygen permeation rates through ion-conducting perovskite membranes, Chemical Engineering Science, 54 (1999) 3839-3850.

[35] M.P. Lobera, S. Escolástico, J.M. Serra, High ethylene production through oxidative dehydrogenation of ethane membrane reactors based on fast oxygen-ion conductors, ChemCatChem, 3 (2011) 1503-1508.

[36] C. Buysse, A. Kovalevsky, F. Snijkers, A. Buekenhoudt, S. Mullens, J. Luyten, J. Kretzschmar, S. Lenaerts, Development, performance and stability of sulfur-free, macrovoid-free BSCF capillaries for high temperature oxygen separation from air, Journal of Membrane Science, 372 (2011) 239-248.

[37] Z. Shao, S.M. Haile, A high-performance cathode for the next generation of solid-oxide fuel cells, Nature, 431 (2004) 170-173.

[38] A. Kovalevsky, C. Buysse, F. Snijkers, A. Buekenhoudt, J. Luyten, J. Kretzschmar, S. Lenaerts, Oxygen exchange-limited transport and surface activation of Ba0.5Sr0.5Co0.8Fe0.2O3-δ capillary membranes, Journal of Membrane Science, 368 (2011) 223-232.

[39] E. Girdauskaite, H. Ullmann, V.V. Vashook, U. Guth, G.B. Caraman, E. Bucher, W. Sitte, Oxygen transport properties of Ba0.5Sr0.5Co0.8Fe0.2O3 - x and Ca0.5Sr0.5Mn0.8Fe0.2O3 - x obtained from permeation and conductivity relaxation experiments, Solid State Ionics, 179 (2008) 385-392.

[40] W.K. Hong, G.M. Choi, Oxygen permeation of BSCF membrane with varying thickness and surface coating, Journal of Membrane Science, 346 (2009) 353-360.

Figure captions

Figure 1 Sketch of the orifice (L/D=0.13) and long (L/D=16) capillaries.

Figure 2 Torque measurements for different volume powder contents.

Figure 3 The reciprocal torque as a function of the PS binder to BSCF powder ratio to calculate the critical powder content.

Figure 4 Equilibrium torque versus powder content.

Figure 5 The graph of apparent shear viscosity versus shear rate for different feedstocks at 180°C.

Figure 6 The pressure versus the shear rate for the three different feedstocks.

Figure 7 Photograph of flat membrane with different powder content after quenching from different temperatures.

Figure 8 The pressure versus the shear rate for feedstock 5 and 6.

Figure 9 Thermogravimetric analysis results for feedstock 6 (heating rate 15°C/min, in air). T5%, T50% and T90% are correspond to 5, 50 and 90% of mass loss.

Figure10 The photograph of the disk and tubes in the different steps.

Figure 11. SEM pictures of planar (A) and tubular (B) after sintered at 1000◦C for 2h.

Figure 12 Grain size distribution of the membranes sintered at 1000°C/2h. The inset is EBSD orientation map together with the corresponding triangle color code: (A) Planar membrane (B) Tubular membrane.

Figure 13 Pole figures for the (0 0 1), (1 1 1) and (1 1 0) axes of the planar and tubular membranes. The color coding indicates the texture index. The values for the maxima remain close to 1.0, indicating a very weak lattice preferred orientation.

Figure 14 Temperature dependence of oxygen permeation flux through the membrane prepared with feedstock 6 (60 vol. % powder content) and 7 (52 vol. % powder content). (Air in the feed stream= 350 Nml/min and different argon flow rates).

Table 1 Characteristics of binders components used in this study.

Binder Component	Density (g/cm^3)	Melting point T_m (°C)	Glass transition temperature T_g (°C)
Stearic acid	0.845	68	-
Polystyrene	1.04	-	100
Paraffin wax	0.91	60	-

Table 2 Formulations of the different feedstocks.

Feedstock	Powder Content (vol. %)	Composition (wt. %)
Feedstock 1	48	82.32 % BSCF Powder, 16.95 % PS, 0.73 % SA
Feedstock 2	52	84.44 % BSCF Powder, 14.81 % PS, 0.75 % SA
Feedstock 3	54	85.41 % BSCF Powder, 13.83 % PS, 0.76 % SA
Feedstock 4	56	86.34 % BSCF Powder, 12.89 % PS, 0.77 % SA
Feedstock 5*	52	86.07 % BSCF Powder, 8.21 % PS, 4.78 % PW, 0.93 % SA

Feedstock 6	60	89.35 % BSCF Powder, 6.11 % PS, 3.56 % PW, 0.98 % SA
Feedstock 7**	52	84.38 % BSCF Powder, 8.21 % PS, 6.47 % PEG, 0.94 % SA

*feedstock 5 was prepared only for comparison of rheological measurements.

** feedstock 7 was prepared only for comparison of oxygen measurements.

Table 3 Characterization of the powders.

Powder	Specific Surface Area (m^2/g)	Median Particle Size (μm)	Pycnometer Density (g/cm^3)	Agglomeration Factor (F_{ag})
Uncoated	1.55 ± 0.01	3.82	5.53 ± 0.00	5.45
Coated	1.16 ± 0.03	2.80	5.25 ± 0.01	2.84

Table 4 Theoretical and pycnometer densities of different feedstocks.

Powder content (%)	Density (g/cm^3)	
	Theoretical	He pycnometer
feedstock 1	3.06	3.10 ± 0.03
feedstock 2	3.22	3.26 ± 0.02
feedstock 3	3.31	3.32 ± 0.01
feedstock 4	3.39	3.40 ± 0.01

Table 5 The reported activation energy values for the $Ba_{0.5}Sr_{0.5}Co_{0.8}Fe_{0.2}O_{3-\delta}$ (BSCF) membranes.

Thickness (mm)	T-range (°C)	Sweep/Feed gas	E_a (kJ/mol)	Limiting step	Ref.
0.8	850-1000	Ar/Air	35	Bulk diffusion	[35]

0.8	700-850	Ar/Air	65	Surface-exchange	[35]
0.4*	850-950	Ar/Air	25	Bulk diffusion	[36]
0.4*	750-850	Ar/Air	44	Bulk diffusion	[36]
1-1.2	390-690	He/Air	113±11	Surface-exchange	[37]
1	800-900	Ar/Air	25-30	Bulk diffusion	[9]
1.5	775-950	He/Air	40.9	Bulk diffusion	[3]
1.5	600-775	He/Air	72.6	Surface-exchange	[3]
0.35-0.45**	850-950	Ar/Air	30.9	Bulk diffusion	[38]
0.35-0.45**	750-850	Ar/Air	52.3	Surface-exchange	[38]
0.5-3	500-700	Ar/Air	71.4±1.2	Surface-exchange	[39]
0.5-3	700-900	Ar/Air	25.8±0.95	Bulk diffusion	[39]
0.75	825-900	He/Air	~17	Bulk diffusion	[40]

* sulfur-free BSCF capillaries

** activated surfaces of sulfur-containing BSCF capillaries with PrO_x

Highlights

- The shape stability of thin membranes during the thermoplastic processing
- An increase in the powder content promotes the shape stability after debinding and sintering processes
- The independence of the oxygen permeation rate from binder system and powder content **at high temperatures**
- No lattice preferred orientation for the tubular and planar membranes

Graphical Abstract (for review)

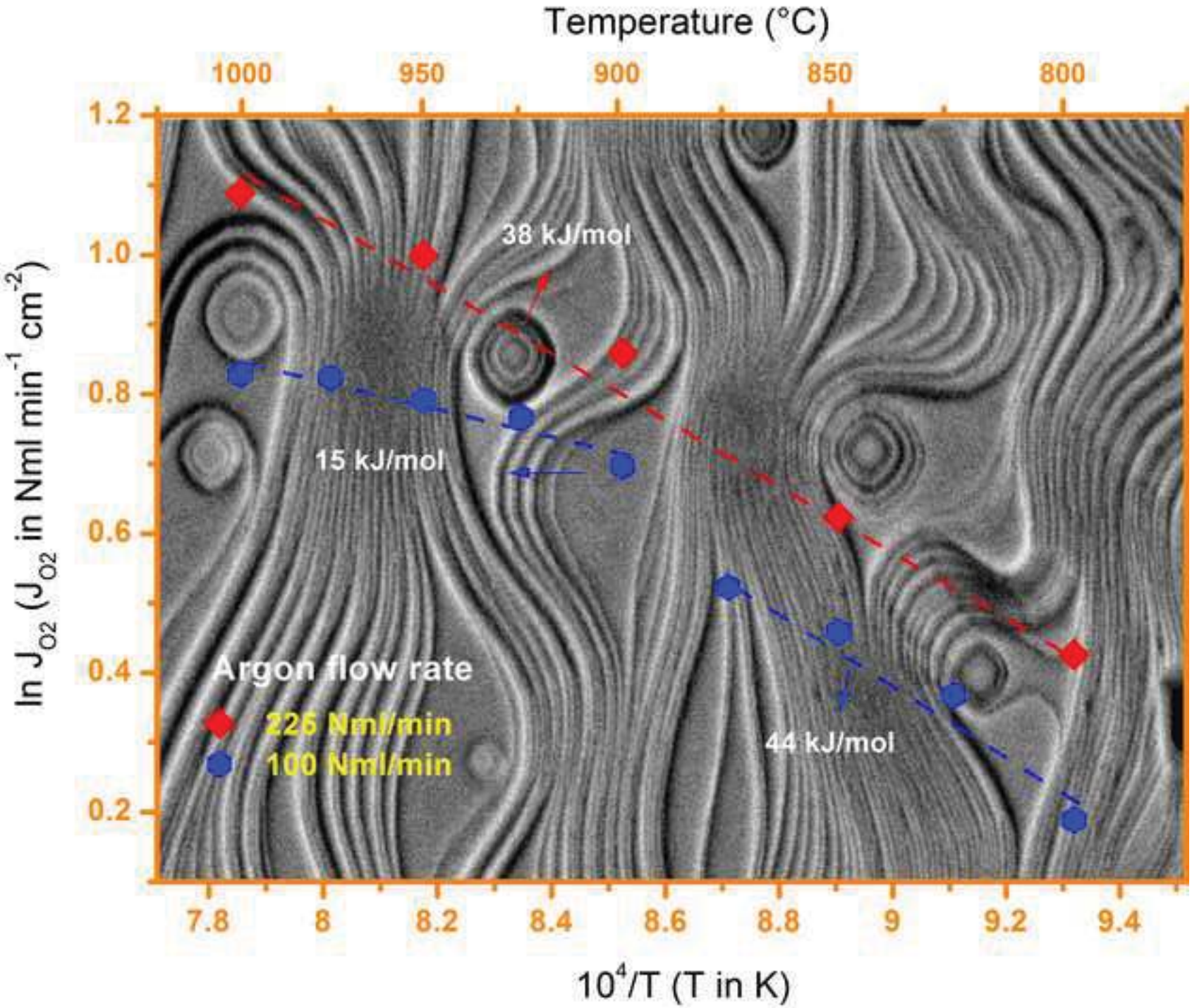

Figure 1

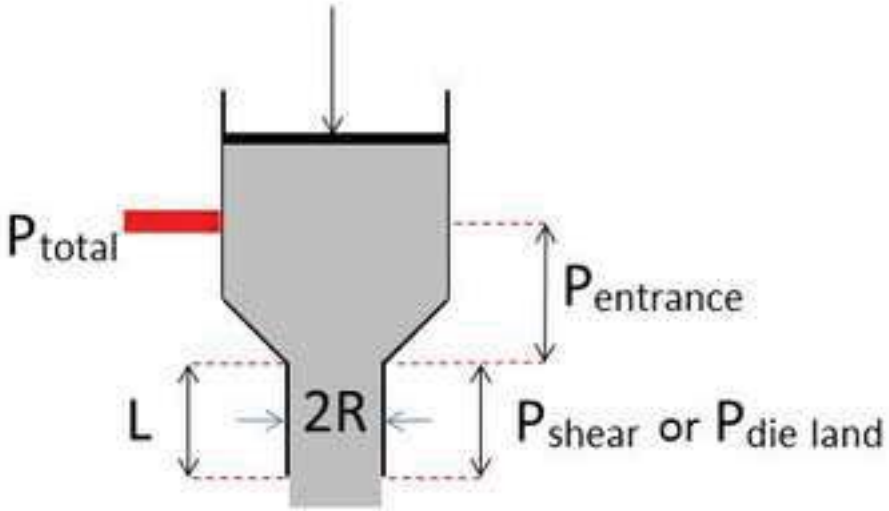

$P_{total} = P_{shear} + P_{entrance}$

long capillary

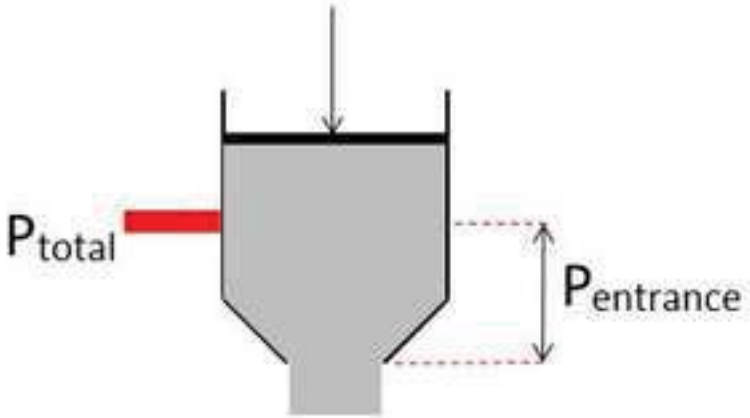

$P_{total} = P_{entrance}$

Orifice capillary

Figure 2

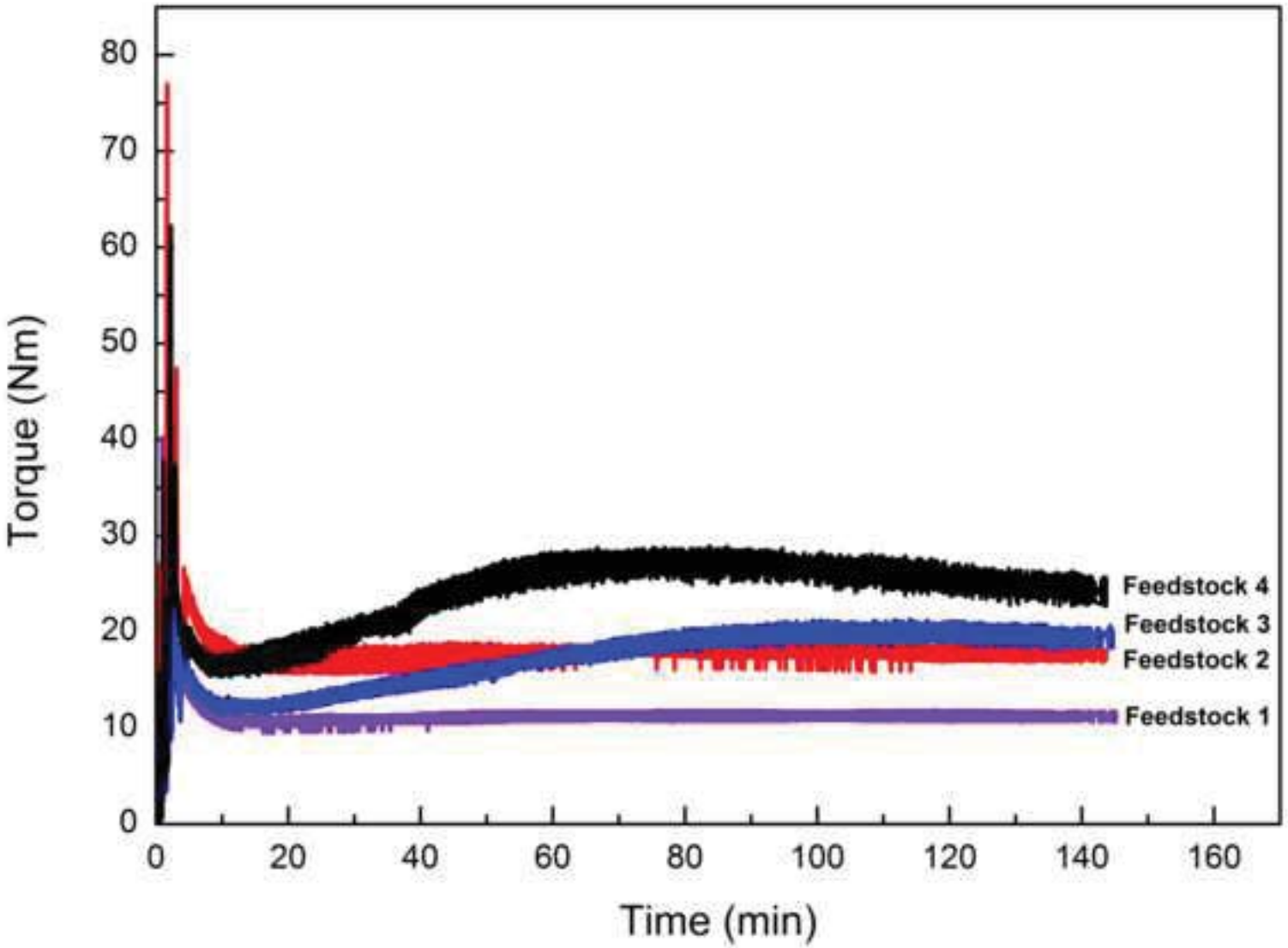

Figure 3

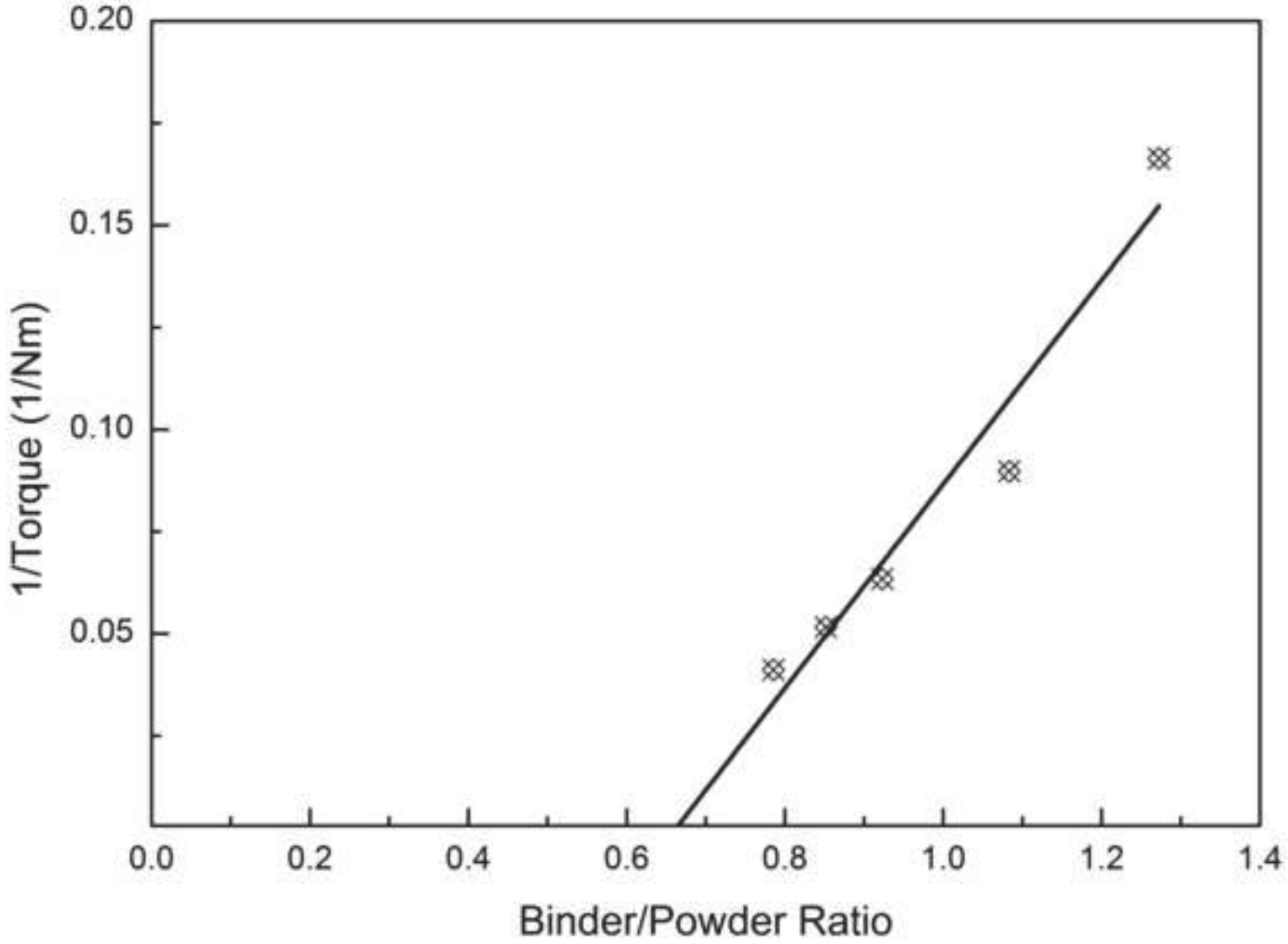

Figure 4

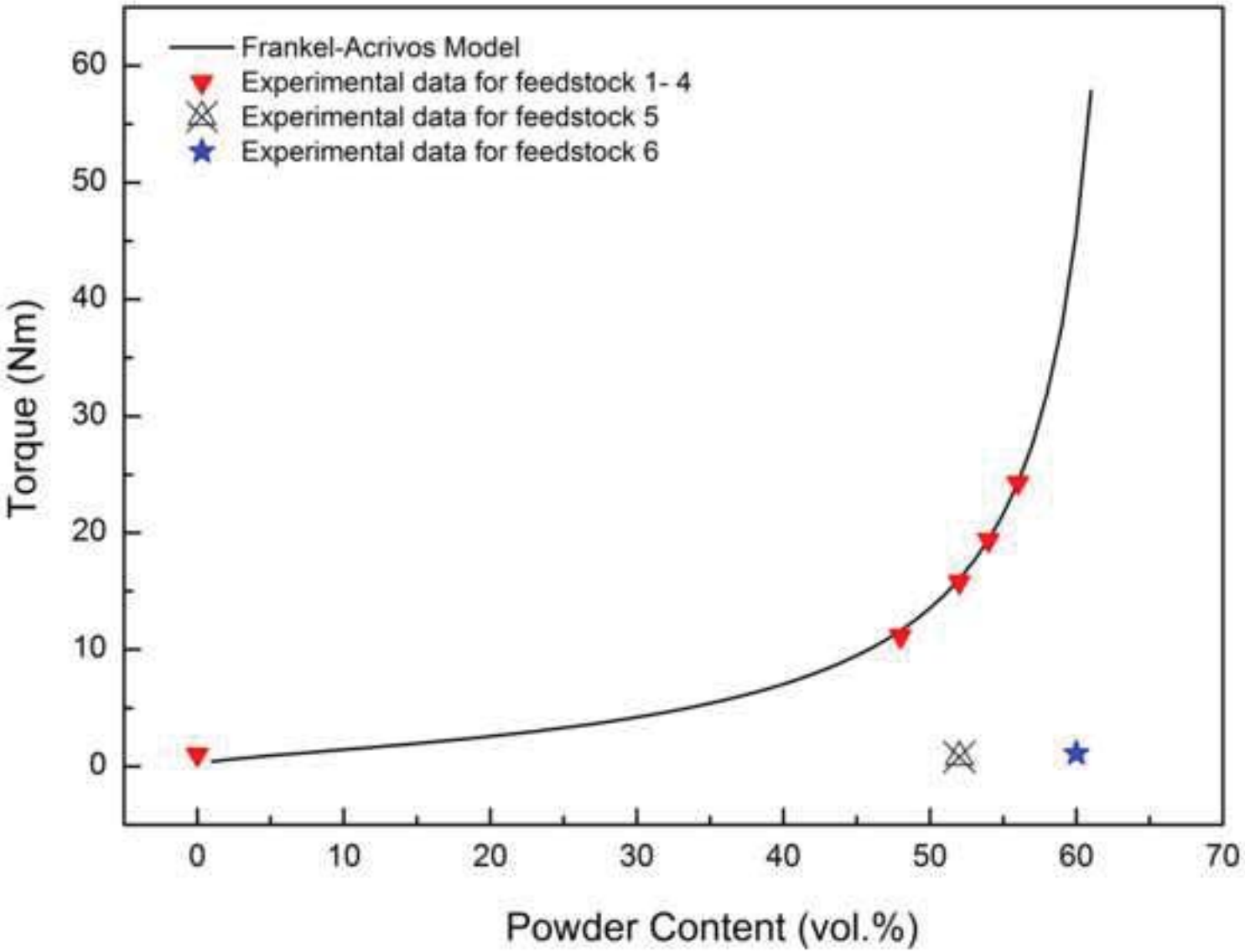

Figure 5

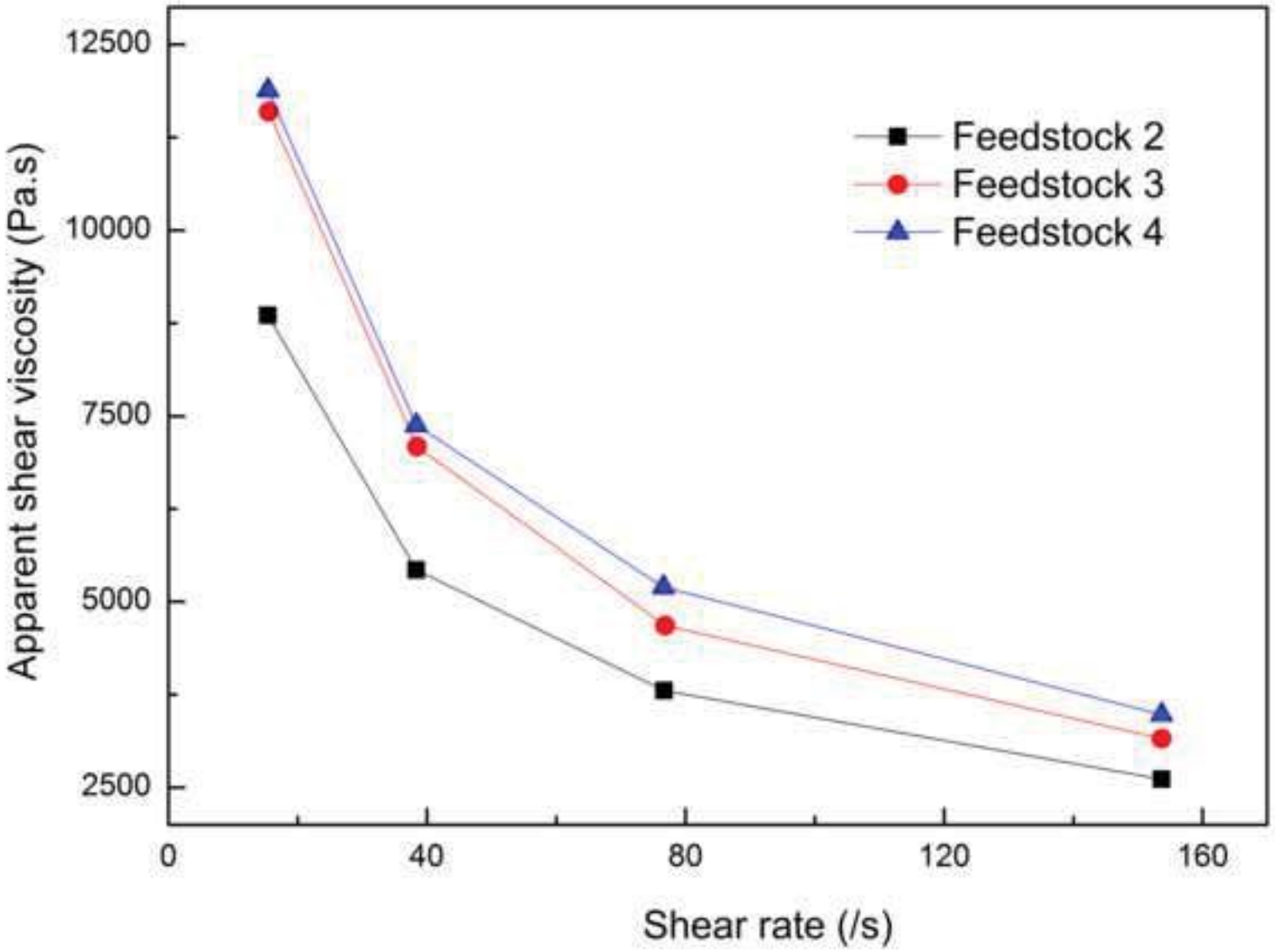

Figure 6

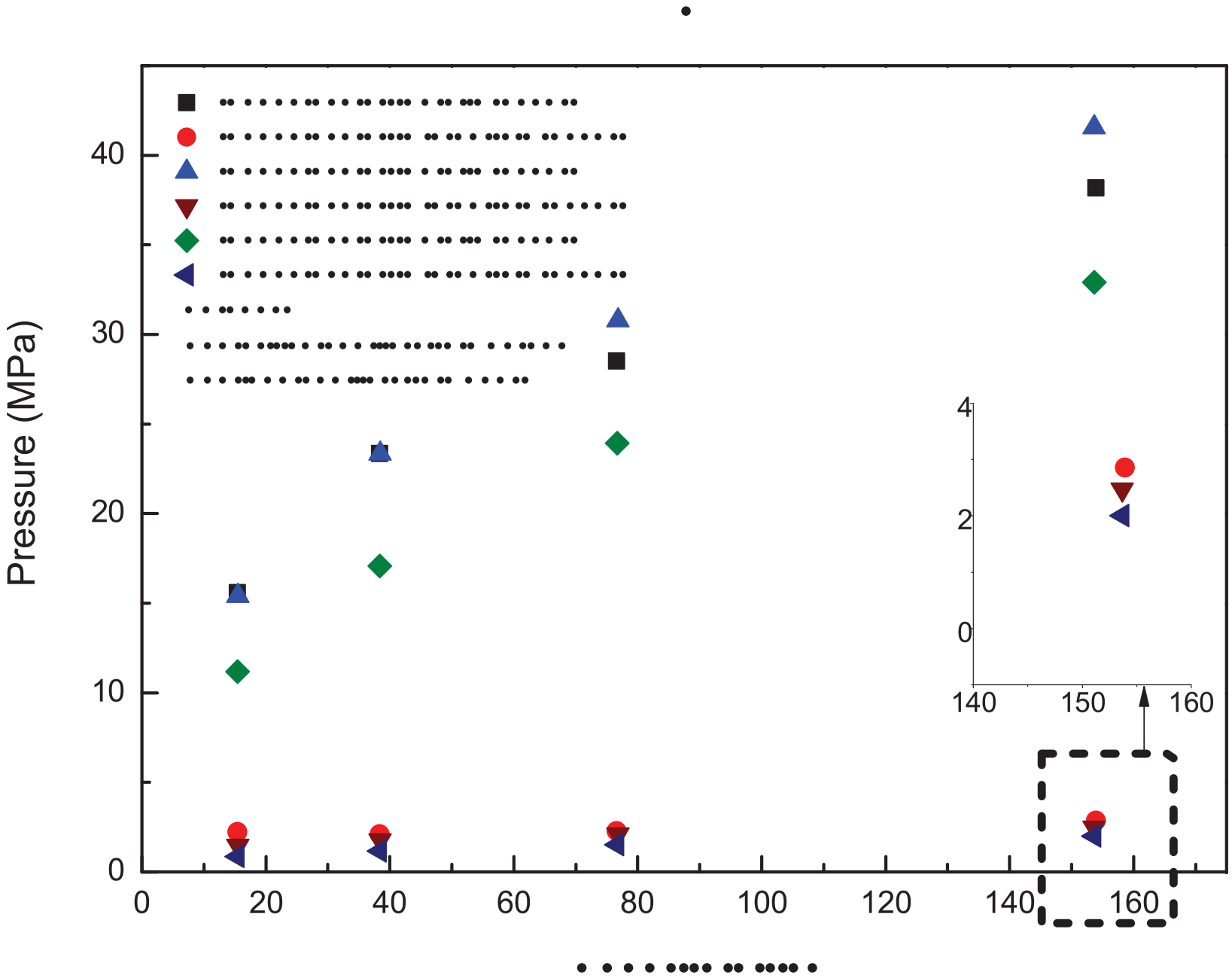

Figure 7

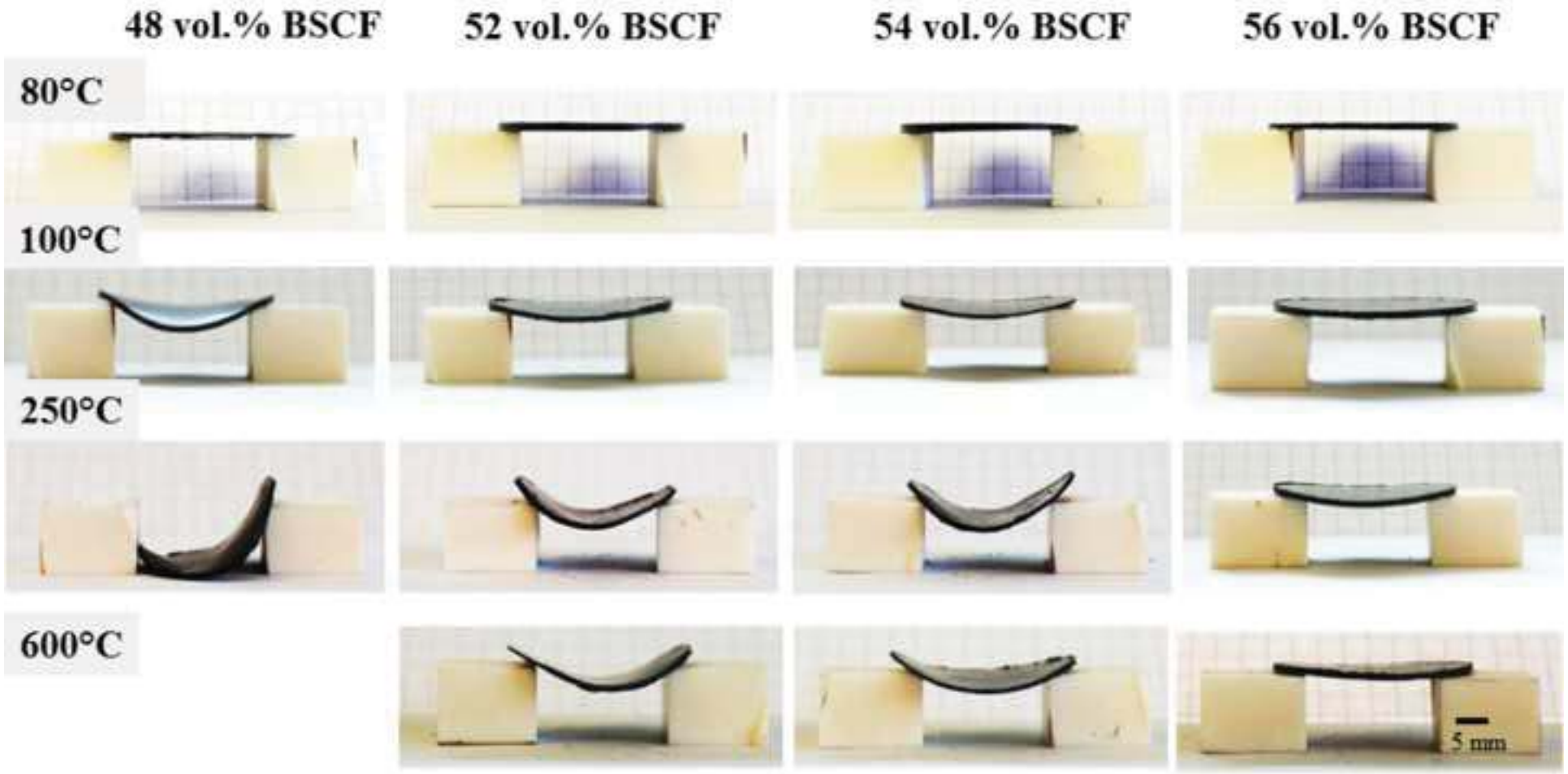

Figure 8

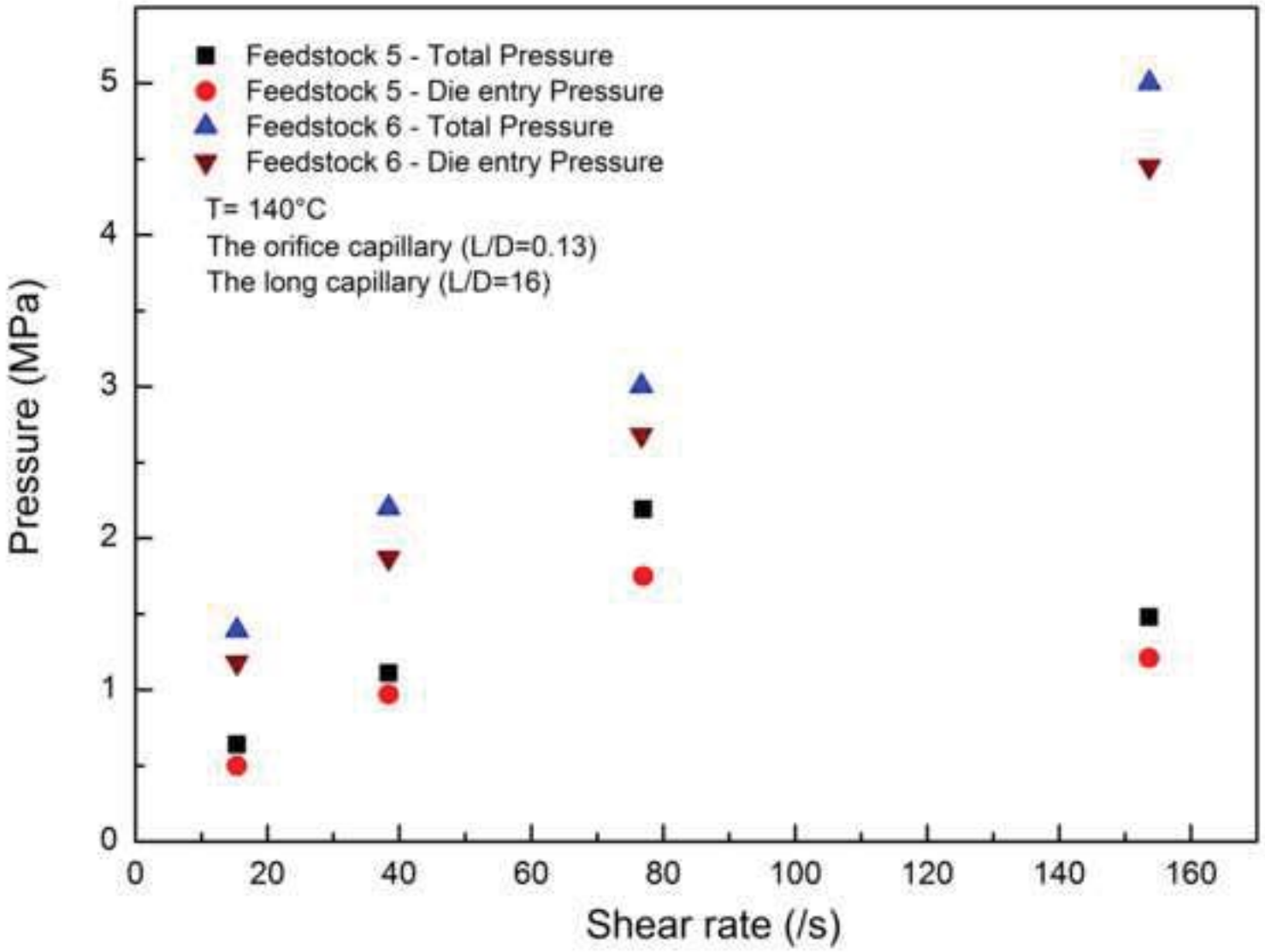

Figure 9

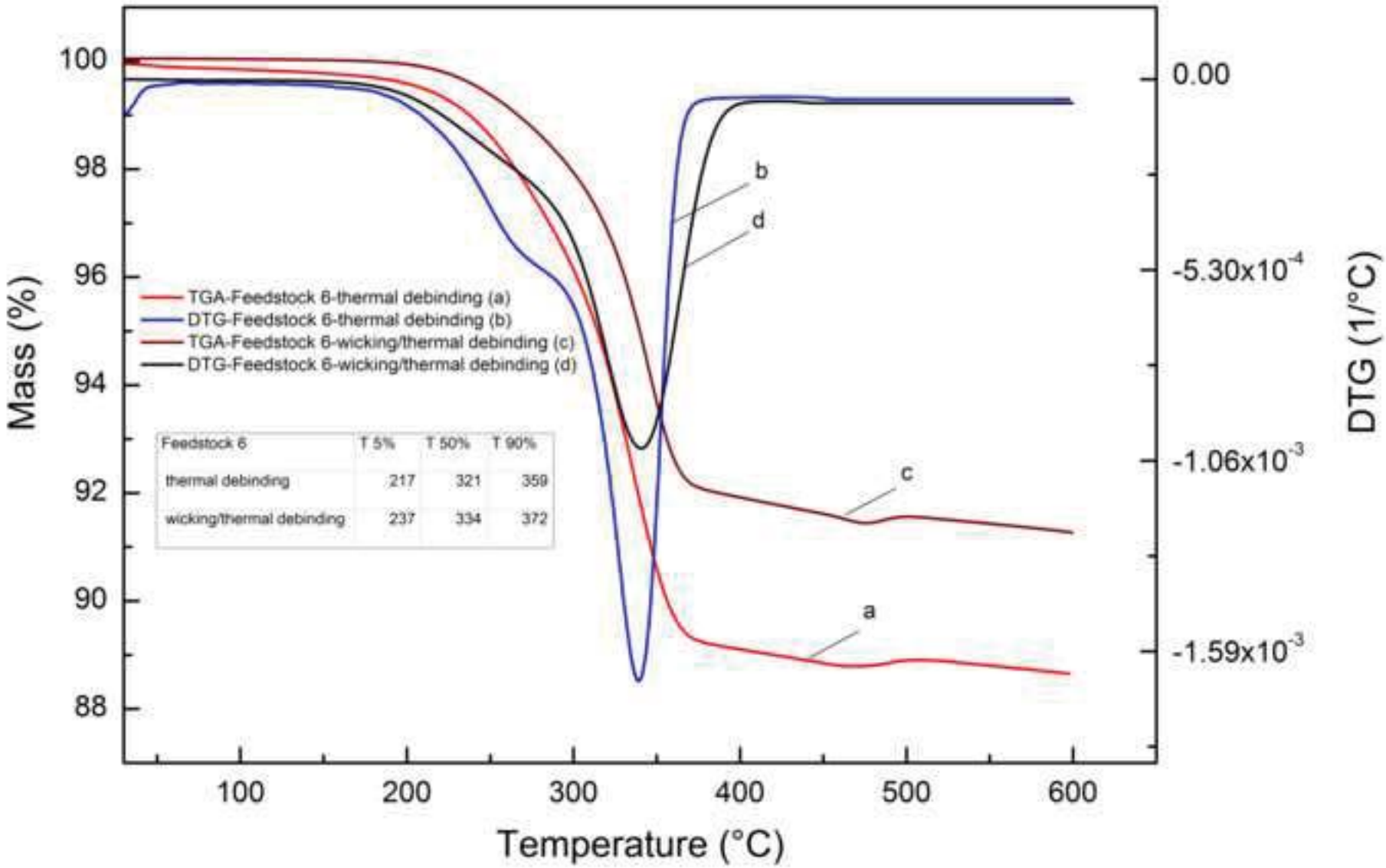

Figure 10

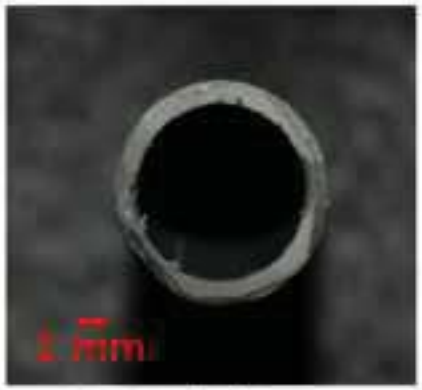

Green tube

Debound tube

Sintered tube

Debound disk

Figure 11

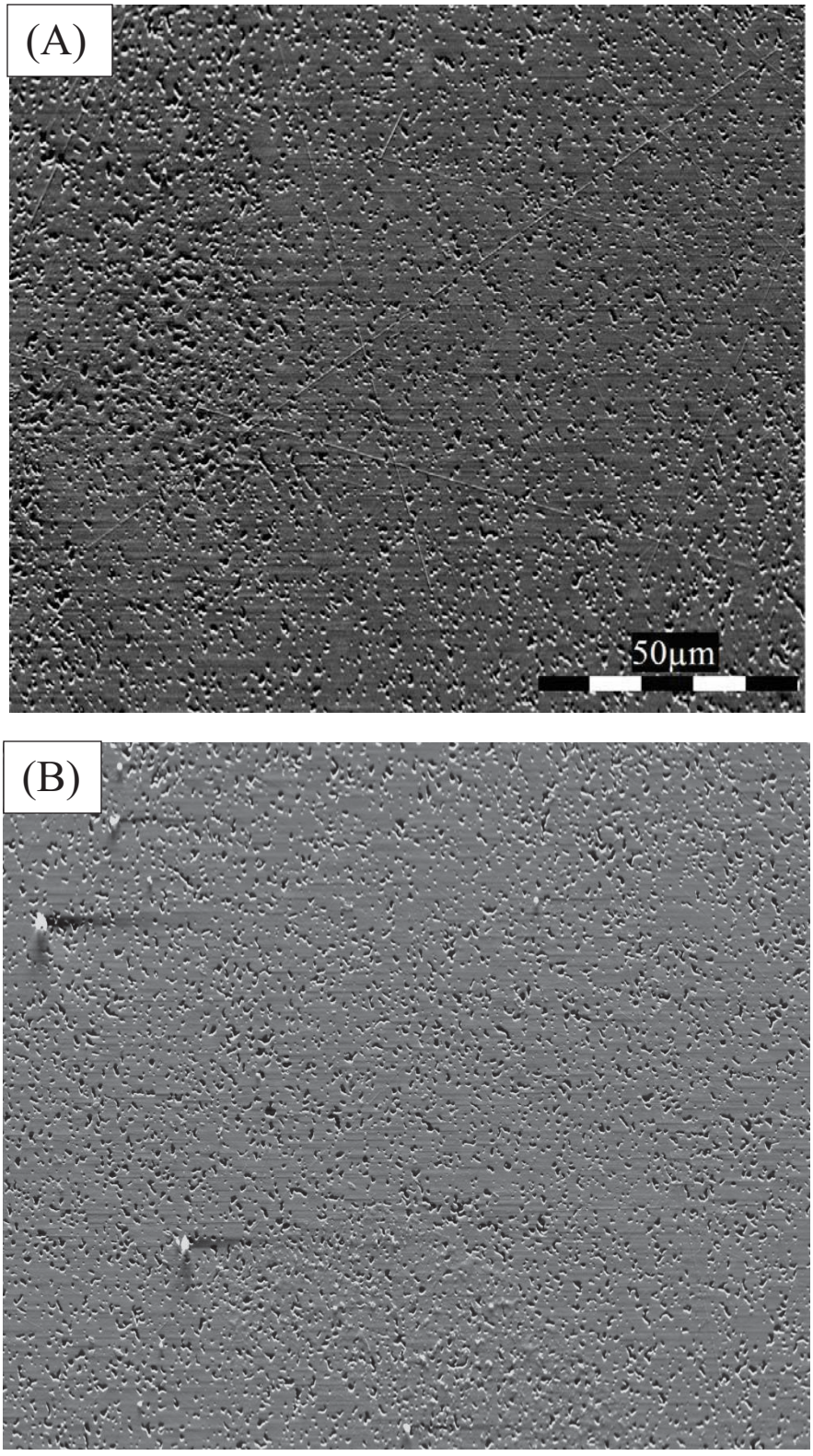

Figure 11. SEM pictures of planar (A) and tubular (B) after sintered at 1000◦ C for 2h.

Figure 12 A Planar membrane

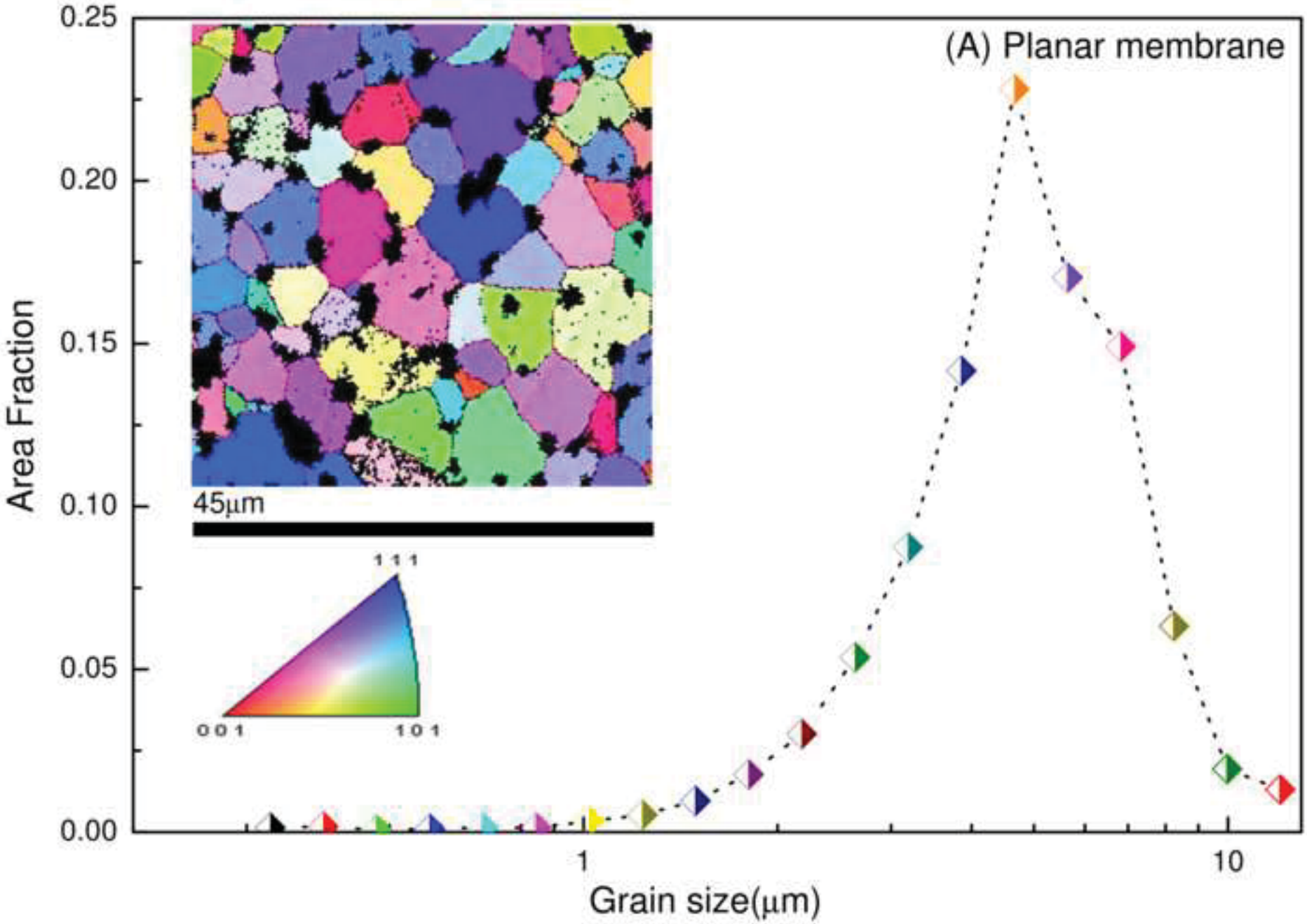

Figure 12 B Tubular membrane

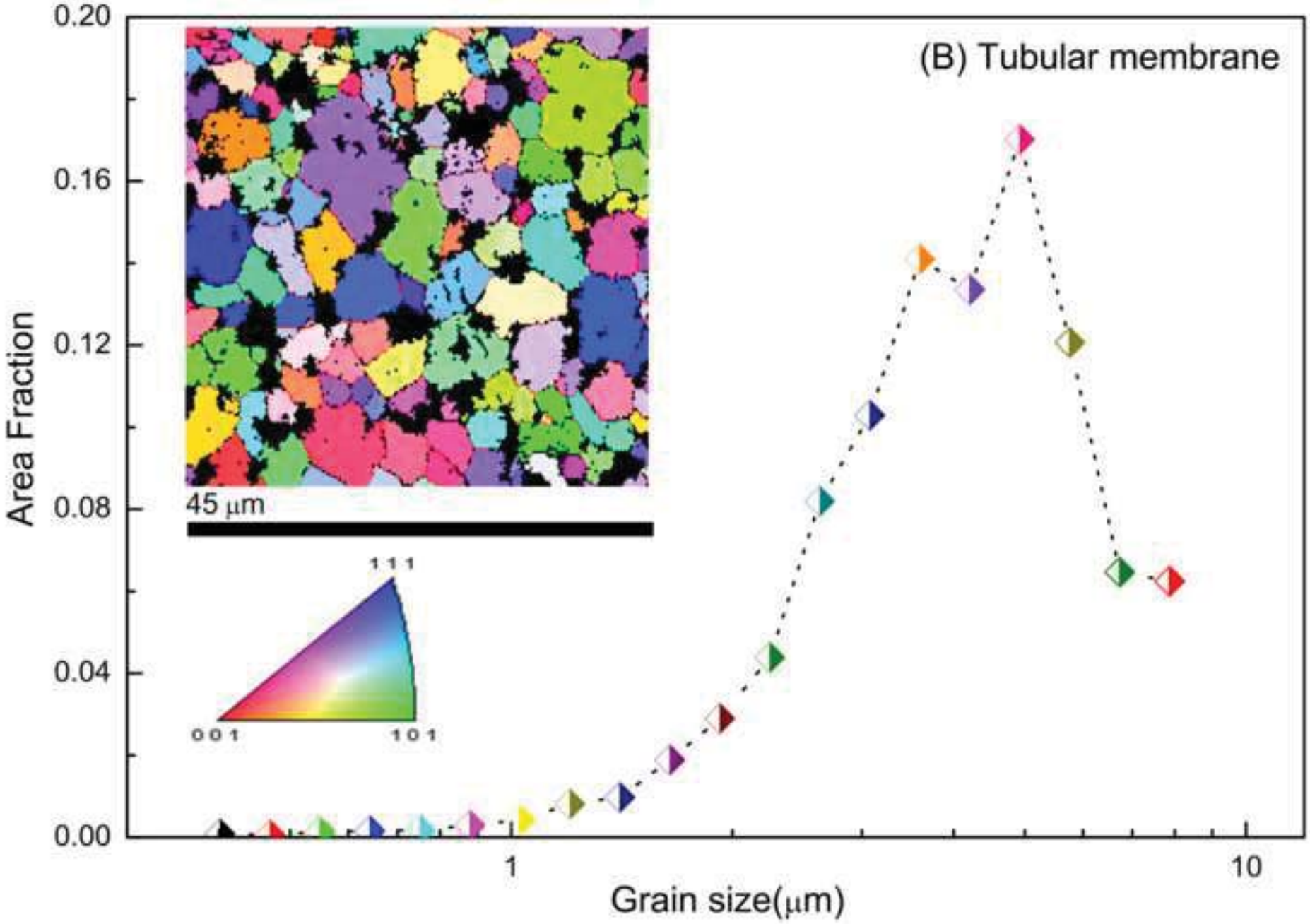

Figure 13 Pole figures

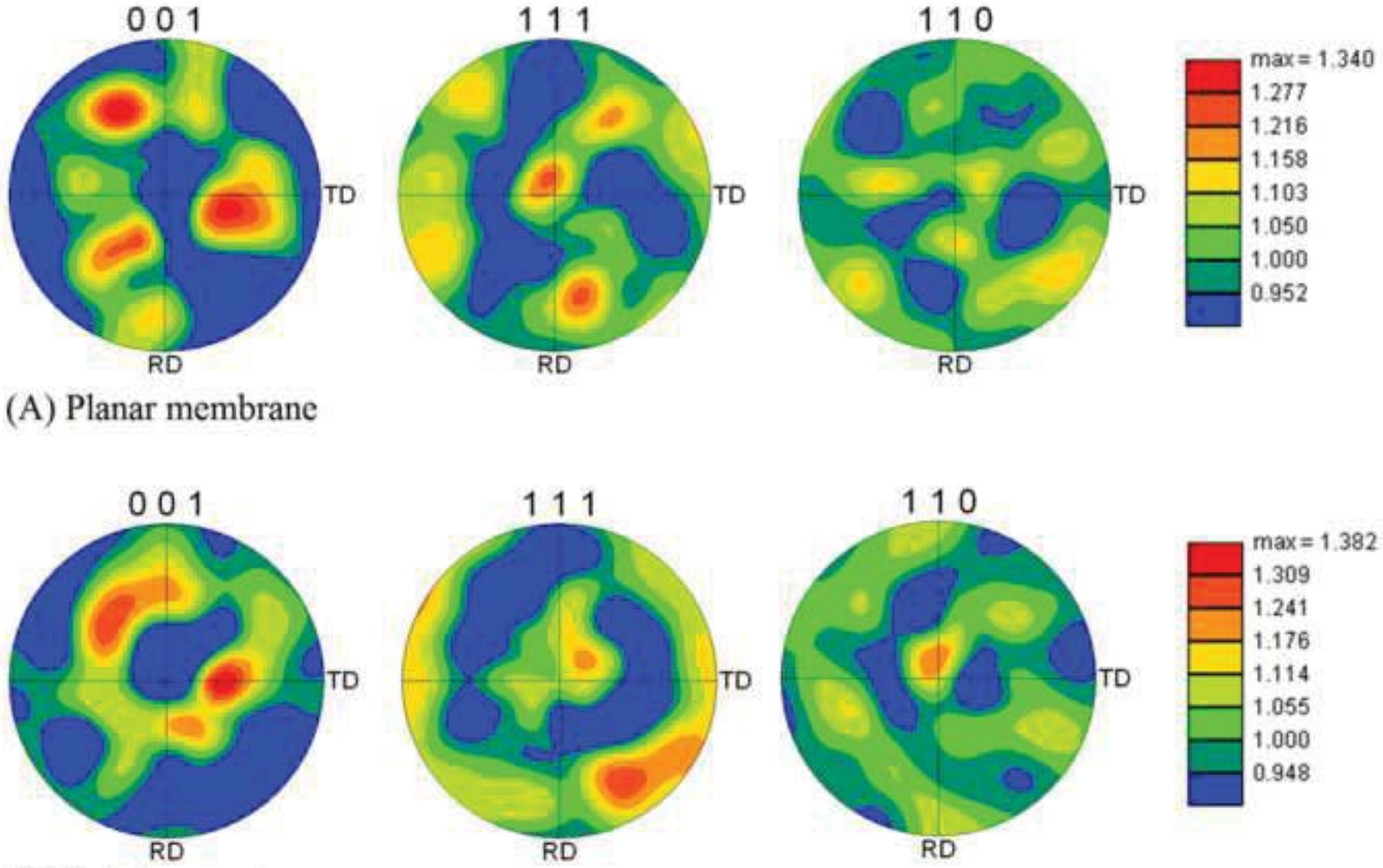

Figure 14